

Partitioned Fluid–Solid Coupling for Cardiovascular Blood Flow: Validation Study of Pressure-Driven Fluid-Domain Deformation

SEBASTIAN KRITTIAN,^{1,2} TORSTEN SCHENKEL,¹ UWE JANOSKE,³ and HERBERT OERTEL¹

¹Institute of Fluid Mechanics, Karlsruhe Institute of Technology, Kaiserstrasse 10, 76131 Karlsruhe, Germany; ²Oxford University Computing Laboratory, Parks Road, Oxford OX1 3QD, UK; and ³Department of Mechanical Engineering, Fluid Mechanics, University of Wuppertal, Gauss-Strasse 20, 42119 Wuppertal, Germany

(Received 31 December 2009; accepted 22 March 2010; published online 2 April 2010)

Associate Editor Kerry Hourigan oversaw the review of this article.

Abstract—The Karlsruhe Heart Model (KaHMo) is a patient-specific simulation tool for a three-dimensional blood flow evaluation inside the human heart. Whereas KaHMo MRT is based on geometry movement identified from MRT data, KaHMo FSI allows the consideration of structural properties and the analysis of FSI. Previous investigations by Oertel *et al.* have shown the ability of KaHMo to gain insight into different intra-ventricular fluid mechanics of both healthy and diseased hearts. However, the *in vivo* validation of the highly dynamic cavity flow pattern has been a challenging task in recent years. As a first step, the focus of this study is on an artificial ventricular experiment, derived from real heart anatomy. Fluid domain deformation and intra-ventricular flow dynamics are enforced by an outer surface pressure distribution. The pure geometrical representation of KaHMo MRT can now be complemented by constitutive properties, pressure forces, and interaction effects using KaHMo FSI's partitioned code-coupling approach. For the first time, fluid domain deformation and intra-ventricular flow of KaHMo FSI has been compared with experimental data. With a good overall agreement, the proof of KaHMo's validity represents an important step from feasibility study toward patient-specific analysis.

Keywords—Cardiovascular blood flow, Fluid–structure interaction, Numerical coupling, Validation experiment.

INTRODUCTION

Cardiac disease is the major cause of death in the western world. To improve diagnosis and therapy methods in the field of surgical treatment of heart failure, the Institute for Fluid Mechanics, University of Karlsruhe, in cooperation with the Department of

Cardio-Vascular Surgery, University of Freiburg, has developed the Karlsruhe Heart Model (KaHMo), a patient-specific blood flow model of the human heart.¹²

In order to investigate the current state of a specific heart from a fluid mechanics point of view, KaHMo MRT represents the MRT-based computational fluid dynamics (CFD) analysis within the human ventricles as described by Schenkel *et al.*¹⁶ The method used for KaHMo MRT is independent of but similar in approach to those presented by Jones and Netaxas,⁴ Baccani *et al.*,¹ and Saber *et al.*¹⁵ Digitized endocardial deformation is used to describe the fluid domain movement of the numerical model. The evaluation of the highly complex intra-ventricular flow pattern has been summarized by Oertel *et al.*¹² and is in good agreement with findings of Kilner *et al.*⁶ and Long *et al.*¹⁰ Walker *et al.*¹⁹ measured the three-dimensional velocity field in multiple planes in the human heart. Pedrizetti and Domenichini¹³ showed that the intake jet generates a ring vortex behind the annular orifice of the mitral valve. Due to lateral displacement of the valve from the ventricle axis and the movement of the myocardium, the vortex grows asymmetrically in time. However, the analysis of the three-dimensional saddle-foci flow topology has only been carried out so far by KaHMo MRT.

Unfortunately, pure fluid domain deformation methods are not able to predict the effects of surrounding structural changes on the intra-ventricular flow-field. In order to provide a multi-physical evaluation process, the simulation of fluid–structure interaction (FSI) becomes of utmost importance. Watanabe *et al.*²⁰ published coupled MRI heart models in which both the fluid and solid domain deforms and the governing equations are solved by a monolithic

Address correspondence to Sebastian Krittian, Oxford University Computing Laboratory, Parks Road, Oxford OX1 3QD, UK. Electronic mail: sebastian.krittian@comlab.ox.ac.uk

method. Earlier studies by Cheng *et al.*² have not only shown the overall potential of this FSI concept, but also a lack in numerical robustness. Penrose and Staples¹⁴ presented a different, partitioned method of fluid–solid coupling based on commercial software using under-relaxation techniques. The novelty of the coupling concept used within this study consists of the multi-physics extension of existing CFD models.⁷ Starting from a KaHMo MRT reference state, KaHMo FSI calculates the ventricular deformation influenced by boundary conditions and structural resistance. The numerical approach as well as the application toward left-ventricular fluid mechanics has been published recently by Krittian *et al.*⁸

The focus of this study is on the validation of the KaHMo FSI concept using results from an artificial ventricle experiment.^{17,18} For the first time, simulation results from KaHMo FSI can be validated experimentally. The ability of KaHMo to represent real cardiovascular flow fields will help to eventually improve surgical treatment and therapy planning from a fluid mechanics point of view.

METHODS

Continuum Mechanics

The continuum mechanics conservation of mass and momentum is given by Eqs. (1) and (2), respectively.

$$\nabla \cdot \mathbf{v} = 0 \quad (1)$$

$$\rho \left[\frac{\partial \mathbf{v}}{\partial t} + (\mathbf{v} - \mathbf{v}_g) \cdot \nabla \mathbf{v} \right] = \nabla \cdot \boldsymbol{\sigma}_{\text{fluid/solid}} \quad (2)$$

If the relative velocity \mathbf{v}_g is equal to the physical velocity \mathbf{v} , a Lagrangian reference system is used. On the other hand, fixed mesh regions where $\mathbf{v}_g = 0$ refer to an Eulerian description. For arbitrary mesh motion ($0 \leq \mathbf{v} \leq \mathbf{v}_g$), the governing equations appear in the so-called Arbitrary Lagrangian–Eulerian formulation. This formulation is valid for both fluid and solid mechanics ($\dot{\mathbf{u}} = \mathbf{v} = \mathbf{v}_g$). The characteristic constitutive properties of each partition are taken into account when defining the Cauchy stress tensor $\boldsymbol{\sigma}_{\text{fluid/solid}}$ for the fluid and solid, respectively. Whereas Stokes theory of liquid friction

$$\boldsymbol{\sigma}_{\text{fluid}} = \frac{1}{3} \text{tr}(\boldsymbol{\sigma}_{\text{fluid}}) \mathbf{I} + \boldsymbol{\tau}_{\text{fluid}} = -p \mathbf{I} + \mu'(\dot{\gamma}) \mathcal{D} \quad (3)$$

yields the fluid mechanical Navier–Stokes equations, a general stress–strain relationship

$$\boldsymbol{\sigma}_{\text{solid}} = \frac{1}{3} \text{tr}(\boldsymbol{\sigma}_{\text{solid}}) \mathbf{I} + \boldsymbol{\tau}_{\text{solid}} = -p \mathbf{I} + \frac{1}{J} \mathbb{F} \frac{\partial W}{\partial \mathbb{E}} \mathbb{F}^T \quad (4)$$

defines the structural equations of motion or balance equations in general. $p \mathbf{I}$ represents the pressure and $\boldsymbol{\tau}_{\text{fluid/solid}}$ the respective deviatoric shear tensors:

- $\boldsymbol{\tau}_{\text{fluid}}$ is defined by the strain rate tensor \mathcal{D} and the viscosity μ' which is a function of the shear rate $\dot{\gamma}$.
- $\boldsymbol{\tau}_{\text{solid}}$ is defined by the strain energy density function W according to the theory of finite elasticity. \mathbb{F} represents the deformation gradient tensor, \mathbb{E} the Green strain tensor, and J the determinant of \mathbb{F} .

Both constitutive relations are defined in the “**Constitutive behavior**” section.

Software

The following sections describe the numerical setup used to both model and simulate the experimental setup. The substantial interaction of blood inertia and low material stiffness is also a challenge in terms of software performance. Partitioned coupling approaches allow packages to be chosen for fluid and solid using specialized numerical simulation features. For the simulation of the flow the software package Fluent 6.3.26²³ is used, whereas the structural mechanical behavior is computed using the finite-element code Abaqus 6.7-1.²² The coupling of these two codes is performed by MpCCI 3.0.5²⁴ which by default represents an explicit coupling scheme. The implicit coupling extension is performed internally by KaHMo FSI.⁸

Partitioned Code-Coupling

Whereas the standard coupling of Fluent, MpCCI, and Abaqus is limited to a single data exchange of load and node position once per time step, the coupling concept used in KaHMo FSI continues a so-called time-step looping, i.e., an iterative data exchange, until the following kinematic (5) and kinetic coupling conditions (6) are satisfied:

$$\mathbf{x}_{\text{fluid}} = \mathbf{x}_{\text{solid}}; \quad \dot{\mathbf{x}}_{\text{fluid}} = \dot{\mathbf{x}}_{\text{solid}}; \quad \ddot{\mathbf{x}}_{\text{fluid}} = \ddot{\mathbf{x}}_{\text{solid}} \quad (5)$$

$$\mathbf{t}_{\text{fluid}} = \boldsymbol{\sigma}_{\text{fluid}} \mathbf{n} = -\boldsymbol{\sigma}_{\text{solid}} \mathbf{n} = -\mathbf{t}_{\text{solid}} \quad (6)$$

$\mathbf{x}_{\text{fluid/solid}}$ denotes the interface position and $\mathbf{t}_{\text{fluid/solid}}$ the stress vector for both fluid and solid domain. The vector \mathbf{n} represents the interface normal vector that points inside the fluid domain. The data exchange itself is performed by MpCCI but then modified within a specialized relaxation procedure: for each time-step j ,

the time-step looping k can use under-relaxation of either node position $\mathbf{x}_{\text{fluid/solid}}$

$$\mathbf{x}_{k,\text{fluid}}^j = \omega_k \cdot \mathbf{x}_{k,\text{solid}}^j + (1 - \omega_k) \cdot \mathbf{x}_{k-1,\text{fluid}}^j \quad (7)$$

or load values $\mathbf{t}_{\text{fluid/solid}}$

$$\mathbf{t}_{k,\text{solid}}^j = \omega_k \cdot \mathbf{t}_{k,\text{fluid}}^j + (1 - \omega_k) \cdot \mathbf{t}_{k-1,\text{solid}}^j \quad (8)$$

A precise description of the coupling algorithm can be found in Krittian *et al.*⁸

Evaluation Methods

The qualitative evaluation procedure used within this study is based on classical streamline techniques, velocity profile evaluation as well as visual consideration of the fluid domain deformation. Dimensionless numbers help to classify cardiovascular fluid mechanics quantitatively and independent of absolute geometric dimension. Reynolds (Re_X^*) and Womersley (Wo_X^*) numbers provide insight into the fluid mechanical ratio of spatial and temporal acceleration, respectively, to flow viscosity forces:

$$Re_X^* = \frac{\rho_B \cdot \bar{u}_* \cdot X}{\bar{\mu}_B}, \quad Wo_X^* = \sqrt{\frac{\rho_B \cdot \omega_0 \cdot X^2}{\bar{\mu}_B}} \quad (9)$$

where ρ_B and $\bar{\mu}_B$ are the blood density and mean viscosity, respectively. \bar{u}_* is a mean inlet/outlet velocity; X is the characteristic inlet/outlet diameter, and ω_0 represents the angular frequency. A dimensional analysis results in further FSI numbers that can be used in order to classify cardiac interaction effects⁸:

$$\begin{aligned} \Pi_{\text{FSI}}^E &= \frac{\rho_B \cdot \bar{u}_*^2}{(W/\hat{V})_{\text{sys/dia}}} \hat{=} \frac{\text{Fluid kinetic energy}}{\text{Solid strain energy}} \\ \Pi_{\text{FSI}}^D &= \frac{(\bar{\mu}_B \cdot \bar{u}_*) \cdot \hat{V}_{\text{sys/dia}}}{W_{\text{sys/dia}} \cdot X} \hat{=} \frac{\text{Fluid diffusive energy}}{\text{Solid strain energy}} \\ \Pi_{\text{FSI}}^A &= \frac{\rho_B \cdot \bar{u}_* \cdot \hat{V}_{\text{sys/dia}}}{W_{\text{sys/dia}}/X} \hat{=} \frac{\text{Fluid acceleration energy}}{\text{Solid strain energy}} \end{aligned}$$

The structural energy densities are represented by $W_{\text{sys/dia}}$. Using the systolic and diastolic cavity volumes V_{sys} and V_{dia} , the specific volumes can be defined as $\hat{V}_{\text{sys/dia}} = V_{\text{ref}} - V_{\text{sys/dia}}$. Referring to the physical mixing process within the heart chamber, the ejection fraction EF, and the mixing parameter M_n shall be defined in percent units as

$$\text{EF} = \frac{V_{\text{dia}} - V_{\text{sys}}}{V_{\text{dia}}}, \quad M_n = (1 - \text{EF})^n \quad (10)$$

Measuring the time t_b until 80% of initial blood has left the heart, O_{pV} allows the dimensionless

representation of the pressure–volume work A_{pV} defined as:

$$O_{\text{pV}} = \frac{A_{\text{pV}} \cdot t_b}{\bar{\mu}_* \cdot (V_{\text{dia}} - V_{\text{sys}})} \quad (11)$$

Particle Image Velocimetry Data Acquisition

The particle image velocimetry (PIV) measurements were carried out at the bio-fluid lab at the Munich University of Applied Science. Green laser ($\lambda = 572$ nm) 2D PIV pictures were acquired as double frame/single exposures with $\Delta t = 250$ – 650 μs . Flow and wall motion were resolved by 18-phase triggered points in time over 1 beat cycle in 4 mm slices. One slice through the valve middle plane was used evaluated in this validation study. Correlation was performed on 32×32 pixel small fields with 50% overlap resulting in an overall resolution of 1.5×1.5 mm^2 .

MODELING APPROACH

Experimental Setup

The KaHMo validation experiment¹⁷ consists of a structurally simplified left ventricle with biological valves between atrium/ventricle and ventricle/outlet. For simplicity, three-flap aortic valves have been used in order to avoid additional inner-ventricular fixation. The initial cavity geometry has been derived from a set of MRT image data of a healthy patient, converted into a reusable negative model filled with resin. The resulting shape has then been covered with an elastic, transparent silicon layer about 1-mm thick. The resin has been melted and the silicon covering is finally obtained as the positive model of ventricle with atrium.

To simulate the human cardiac cycle from a fluid mechanics point of view, we placed the silicon model inside a pressure chamber which is shown on the left-hand side of Fig. 1. Removing liquid periodically from the pressure chamber forces the elastic ventricle by suction to inflate from its end-systolic position to the end-diastolic volume. Table 1 summarizes further model characteristics.

The circulatory resistance is represented by two throttles which enforce a non-physiological absolute pressure. However, the intra-ventricular fluid mechanics is not affected by the environmental pressure since only relative distributions are taken into account. Moreover, from a solid mechanics point of view, it is only the difference of absolute pressures (inside and outside the cavity) that causes the fluid domain deformation. All liquids in the measuring

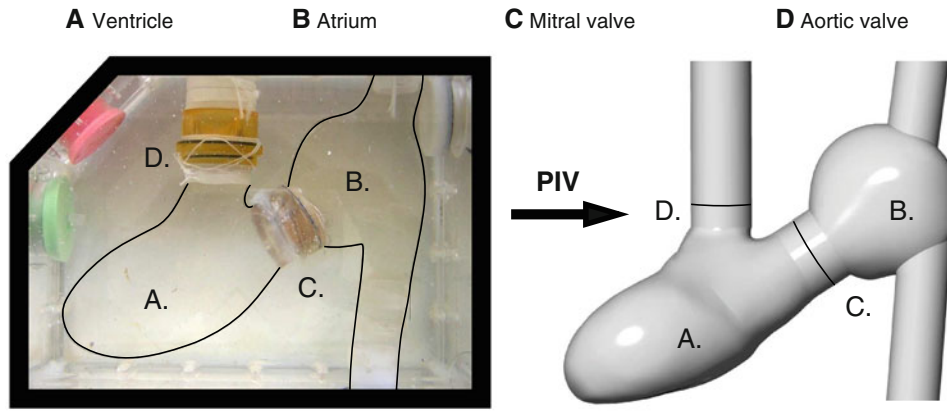


FIGURE 1. Experimental setup and geometrical representation for $\varphi_{17} = 345^\circ$.

TABLE 1. Validation model characteristics.

Model properties	Symbol	Unit	Value
Diameter mitral valve	D_M	mm	15
Area mitral valve	A_M	mm ²	177
Atrium pressure level	ρ_M	mbar	85
Diameter aortic valve	D_A	mm	14
Area aortic valve	A_A	mm ²	156
Aorta pressure level	ρ_A	mbar	95
Density	ρ_B	kg/m ³	1008
Viscosities	μ_0/μ_∞	mPa s	13.15/3.00

chamber as well as the elastic ventricle wall have approximately the same refractive index. This is particularly important for the following determination of velocity distributions with optical measurement such as PIV.

Numerical Model

The CAD geometry on the right-hand side of Fig. 1 has been derived as a by-product of the sequenced PIV measurement planes. It describes the initial stress-free configuration slightly altered due to the surrounding liquid distribution. Figure 2 shows the meshes used for the fluid and solid discretizations. Due to a limited atrium movement, the structural representation covers the cavity volume only, whereas the fluid space takes the entire CAD geometry into account. The cavity model consists of 200,000 tetrahedron cells, whereas the silicon structure is discretized by 10,000 linear shell elements. The fluid mesh size has been determined as sufficiently fine in an *a priori* mesh-dependence study in which both mesh size Δx and time-step size Δt have been varied in constant ratio. The numerical stability criteria ($CFL = \mathbf{v} \cdot \Delta t / \Delta x \approx 1$) guarantees a sufficient resolution for representing the physical velocity \mathbf{v} . With a 2-mm mesh size, characteristic values (e.g.,

inflow and outflow velocities, vorticity, viscosity, and pressure) show a converged representation KaHMo.⁷ The shell element discretization has been chosen in respect to the mapping of partner cells at the common interface.

Mitral and aortic valves are reproduced by KaHMo's two-dimensional projection onto the valve plane.¹⁶ Opening area, pressure distribution, and ventricular volume have been identified from experimental data and can be represented in a time-synchronized manner. Figure 2 shows the restricted area of 100, 90, and 82% for the inlet valve; the outlet valve opens with a restricted area of 100, 86, and 62%. The incomplete opening of the valves is due the limited power of the pump.

For the fluid solver an Euler implicit time stepping scheme and a second-order spatial discretization have been used which allow both mesh movement and cell quality-based re-meshing. In the case of intra-ventricular FSI, structural inertia can be neglected compared to the effect in fluid flow⁷ and an implicit quasi-steady solver scheme has been applied for the solid domain with quadratic basis functions. One heart cycle is discretized into 200 time-steps.

For the further evaluation process it should be noted that both KaHMo FSI and KaHMo MRT use identical geometrical representation and numerical schemes. However, for KaHMo MRT imposing the geometry movement requires the replication of the model building process for each recorded time-step. More sophisticated preparation strategies have been published previously by Schenkel *et al.*¹⁶

Constitutive Behavior

The ventricular model used for the experimental setup is filled with dimethyl sulfoxide with the same non-Newtonian properties as blood. The Cauchy stress

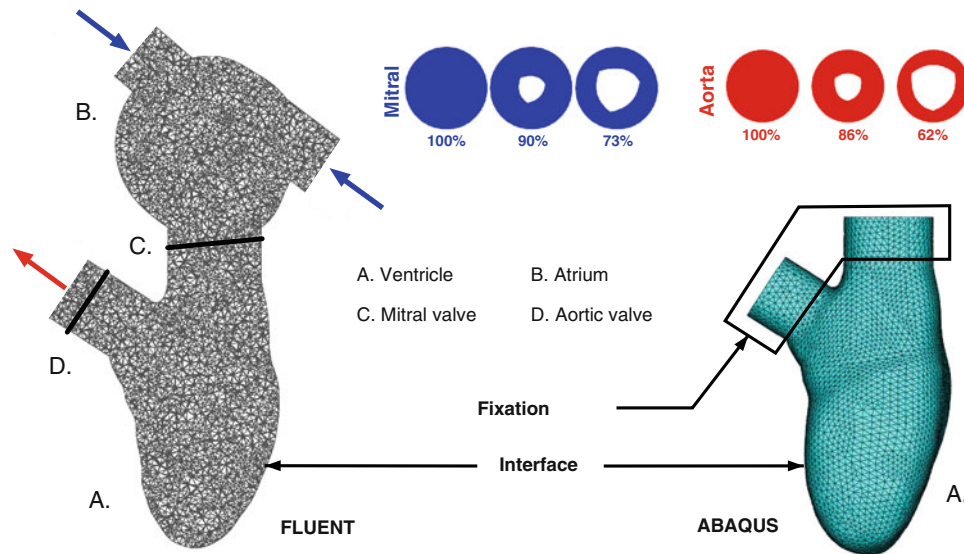


FIGURE 2. Domain discretization of the fluid–solid coupled validation model.

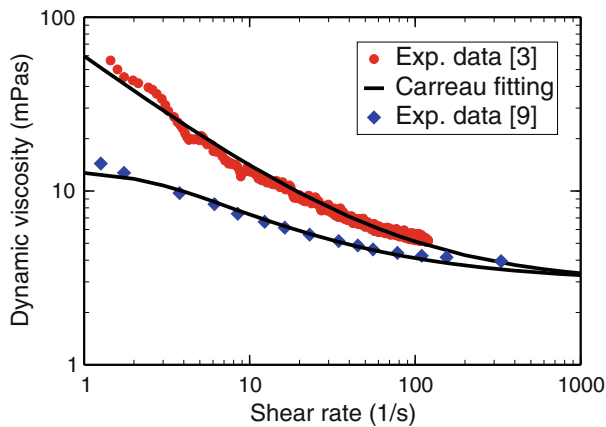


FIGURE 3. Experimental viscosity data and Carreau approximation.

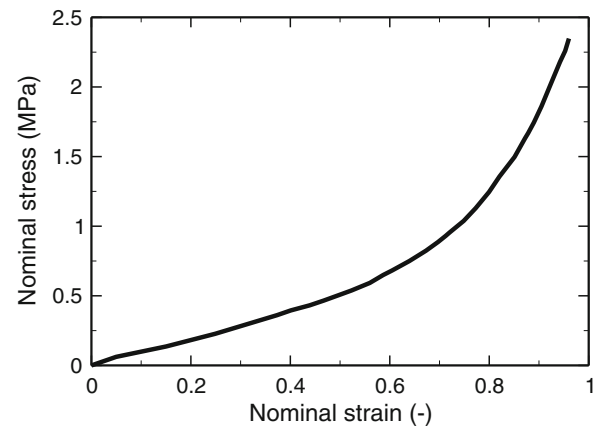


FIGURE 4. Uni-axial data for the structural constitutive behavior.

tensor σ_{fluid} within a general fluid mechanics context is given by Eq. (3).

Due to the non-Newtonian behavior of blood flow, the Carreau-Model³ shall be used to fit different conditions of blood viscosity as shown in Fig. 3.

$$\mu' = \mu_{\infty} + (\mu_0 - \mu_{\infty}) \cdot \left[1 + (\lambda \cdot \dot{\gamma} \cdot k_T)^2 \right]^{\frac{n-1}{2}} \quad (12)$$

The parameters $n = 0.4$ and $\lambda = 0.4$ as well μ_0 and μ_{∞} are based on isothermal condition $k_T = 1$ and can be adapted to the application under consideration.

With the focus on the cavity flow pattern rather than on wall stress distributions, a shell-like structural representation is sufficient as long as the uni-axial

stress–strain relationship is comparable to homogenized and mean averaged myocardial tissue.

Figure 4 plots the stress–strain relationship of the artificial ventricular model to illustrate its highly non-linear constitutive properties needed for specifying σ_{solid} in Eq. (4).

Boundary and initial conditions

The deformation in the simulation model is a direct response to the absolute pressure difference between the inside and outside of the ventricle. It should be noted that the absolute pressure level of the experimental setup does not affect the flow inside the ventricle as this is determined by pressure differences only.

Consequently, inlet and outlet pressure boundary conditions can be set to zero in respect to the environmental pressure of 8.5 and 9.5 kPa in diastole and systole, respectively. Figure 5 shows the time-dependent pressure distribution of the chamber measurements. Starting with the stress-free reference state, the contraction of the model ventricle is followed by the actual expansion which results in a pressure drop inside the chamber. The corresponding pressure boundary condition acting on the structural wall can be defined as a function of the cycle-specific t^* with

$0 < t^* = t/T_0 < 1$ with an integrated error of less than 5%:

$$\begin{aligned}
 &0.0 < t^* \leq 0.6: \\
 &p = 0.25 \text{ kPa} \\
 &\quad - 11.00 \text{ kPa} \cdot 0.5 \cdot \left(1 - \cos\left(\frac{5\pi \cdot t^*}{3}\right)\right) \\
 &0.6 < t^* \leq 1.0: \\
 &p = -10.75 \text{ kPa} \\
 &\quad + 11.00 \text{ kPa} \cdot 0.5 \cdot \left(1 - \cos\left(\frac{5\pi \cdot t^* - 3\pi}{2}\right)\right)
 \end{aligned} \tag{13}$$

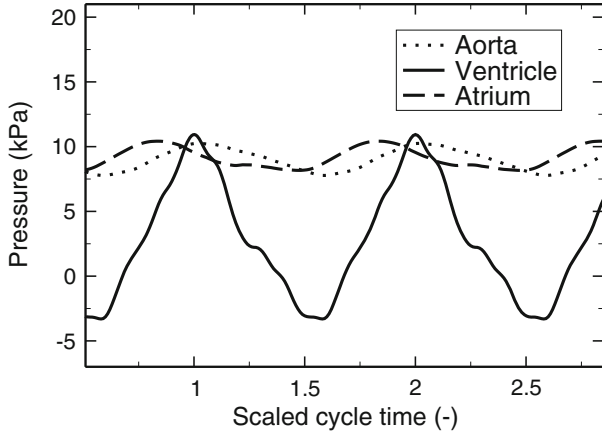


FIGURE 5. Measurement data of chamber and system pressure.

Note, that both the experimental setup as well as the simulation model need to perform several cycles in order to guarantee that a repeatable flow is obtained. This convergence is confirmed by the quantitative values in Table 2 which build the basis for a subsequent evaluation of both mixing rate and mixing time.

RESULTS

For the first time the simulation data of KaHMo FSI can be compared not only with KaHMo MRT, but also with experimental measurements for validation purposes. The following section focuses on global pressure and volume changes as a result of the geometrical deformation history. Finally, numerical simulation results are evaluated both qualitatively and quantitatively by visualization and dimensional analysis.

TABLE 2. Quantitative evaluation and dimensionless numbers of KaHMo FSI, KaHMo MRT, and the experimental setup.

	Symbol	Unit	FSI	MRT	EXP
Volume					
End-systolic volume	V_{sys}	mL	142.53	143.64	142.73
End-diastolic volume	V_{dia}	mL	192.30	191.74	193.30
Stroke volume	V_{S}	mL	49.77	48.10	50.57
Cycle time	T_0	s	1.00	1.00	1.00
Pulse	HR	1/min	60	60	60
Systolic time	t_{sys}	s	0.43	0.43	0.44
Diastolic time	t_{dia}	s	0.57	0.57	0.56
Mean flow characteristics					
Aortic velocity	\bar{v}_{sys}	m/s	0.74	0.72	0.75
Mitral velocity	\bar{v}_{dia}	m/s	0.49	0.47	0.51
Viscosity	$\bar{\mu}_{\text{eff}}$	g/(m·s)	5.23	5.45°	5.50
Pump characteristics					
pV work	A_{pV}	J	0.11	0.09	—
Performance	P_{pV}	W	0.11	0.09	—
Ejection fraction	EF	%	25.88	25.09	26.16
Mixing coefficients					
	M_1/M_2	%	70.6/50.3	71.4/51.1	—
	M_3/M_4	%	35.7/25.2	36.1/25.8	—
	M_5/M_6	%	17.8/12.6	18.6/13.2	—
Mixing time	$t_{b,20}$	s	4.35	4.47	—

Positioning and Volume Changes

As a by-product of the PIV measurement, slices perpendicular to the axial direction and spaced by 5 mm are obtained at every phase φ_i from which the recording time t_i can be derived as follows

$$t_i = \frac{\varphi_i}{360^\circ} \cdot T_0 = \frac{20^\circ \cdot i + 5^\circ}{360^\circ} \cdot T_0 \quad (14)$$

where $i = 0, 1, 2, \dots, 17$ and T_0 defines the cardiac cycle time with $0 < t^* < T_0 = 1$ s. Each phase allows the reconstruction of a geometrical model with an estimated volume error of less than the estimated measurement error of 10%. Whereas KaHMo MRT uses all 18 phase geometries for providing the grid motion, KaHMo FSI uses phase $\varphi_{17} = 345^\circ$ as a reference geometry, shown previously in Fig. 1.

To evaluate the spatial deformation of KaHMo FSI in more detail, simulated and measured geometries are compared for characteristic time-frames from end systole to end diastole (see Fig. 6). The superposition of the smallest ($\varphi_0 = 5^\circ$), the largest ($\varphi_5 = 105^\circ$), as well as an average-sized ventricle shape ($\varphi_{10} = 205^\circ$) for the filling phase shows a very good agreement. The dashed line indicates the measured geometry, whereas the full line indicates the simulation result. As

expected, the normalized root mean square error for the spatial positioning increases from early-to-end diastole but remains much smaller than the estimated measurement error.

From a fluid mechanics point of view, the subsequent evaluation of the inner-ventricular flow pattern is influenced significantly by the inflow jet. With a correct representation of the opening area, the inflow jet velocity is a direct response to the function plotting cavity volume over time. One can clearly see an excellent overall agreement of both simulated and measured volume over time. However, regarding the evaluation points shown in Fig. 7 one must note that there is a slight discrepancy for $\varphi_5 = 105^\circ$ which, presumably, can be attributed to fluid inertia effects.

Pressure–Volume Relationship

The pre and post-ventricular pressures are a result from pump pressure, circulatory resistance, and fluid inertia and have an averaged value of approximately 15 kPa. The level of inlet and outlet pressure results from the calibration of the circulatory device. This level represents the initial pressure and can consequently be regarded as environmental pressure.

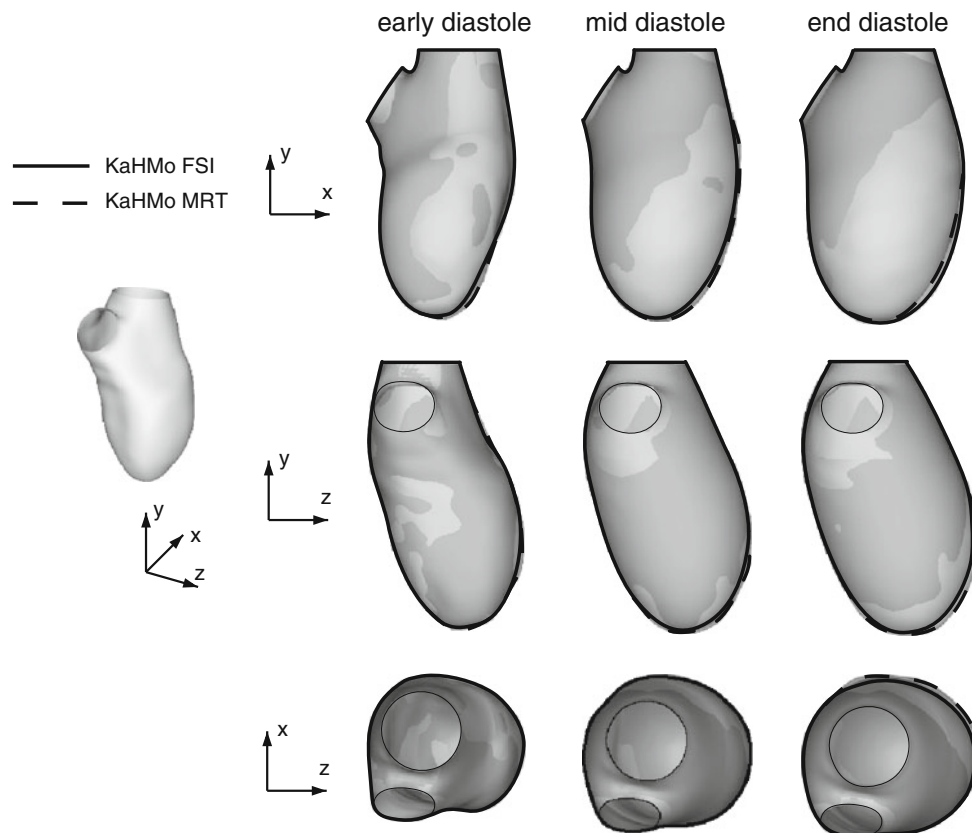


FIGURE 6. KaHMo FSI and KaHMo MRT deformation of the fluid domain for the phases $\varphi_0 = 5^\circ$, $\varphi_5 = 105^\circ$, and $\varphi_{10} = 205^\circ$.

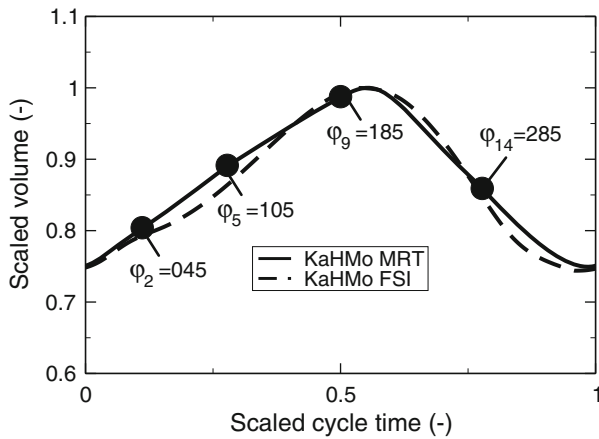


FIGURE 7. Cavity volume of KaHMo FSI and KaHMo MRT over time.

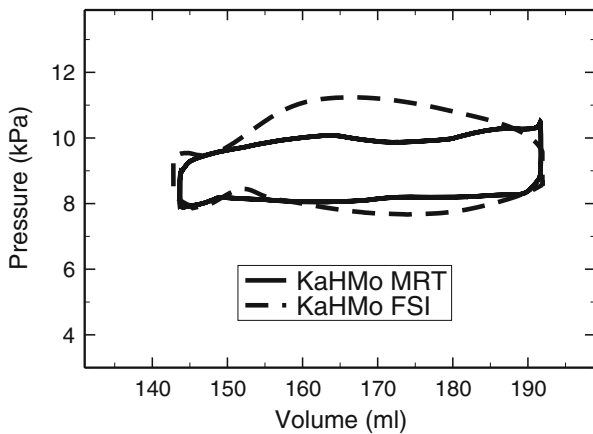


FIGURE 8. Cavity pressure of KaHMo MRT and KaHMo FSI over volume.

In Fig. 5 we can see the intersections of outer- and inner-ventricular pressure which corresponds to the opening and closing time of inlet and outlet with some delay due to inertia effects. It can be seen that the suction phase takes up 60% of the cycle time, whereas the pressure phase takes up to 40%. In Fig. 7, however, the ratio of intake flow to output flow is reduced by inertia effects to 55 to 45%.

These inertia effects can also be observed in Fig. 8 which represents the amount of pressure work that is needed to overcome the pressure–volume change. It must be noted that KaHMo FSI delivers a substantial contribution to the actual pump work in contrast to KaHMo MRT which is limited to the information about the relative change of dynamic pressure. As a reaction to the boundary conditions measured within the experimental setup the coupling model exhibits interaction between internal forces and the pressure acting on the structure of the model ventricle. On the left-hand side of Fig. 8—in the vicinity of the smallest ventricle volume—a wave-shaped pressure reaction can

be seen, which is due to the buckling of the shell model also observed during the real experimental sequence.

Inner-Ventricular Flow Field

The PIV measurements of the validation experiment permit the quantitative recording of the velocity distribution within the model ventricle, as well as the visualization of the flow field. The experimental results are then discussed at the characteristic evaluation phases $\varphi_2 = 45^\circ$, $\varphi_5 = 105^\circ$, $\varphi_9 = 185^\circ$, and $\varphi_{14} = 285^\circ$ of Fig. 7 and compared with the KaHMo MRT and KaHMo FSI results in Figs. 9–12.

Phase $\varphi_2 = 45^\circ$ corresponds to an early stage of the intake process. It can be seen from Fig. 9 that both simulation models correspond nicely to the flow structure of the validation experiment. The intake jet is accompanied by a torus-shaped ring vortex. The left part of the vortex appears to be fixed in position due to the spatial arrangement of the aortic channel. Moreover, there is a good representation of the flow structure in the atrium and apex of the heart.

At later instances of the cycle, the deep penetration of the intake jet into the ventricle at phase $\varphi_5 = 105^\circ$ (Fig. 10) can be seen. The figure shows the streamlines through the mitral and aortic valves projected on a plane defined by points in the center of inlet and outlet as well as the heart tip. The right part of the ring vortex moves to the edge of the fluid space in the direction of the apex of the heart, whereas the left part grows in the upper position. At this point in time there is a good agreement with the flow structure in the atrium as well as the cavity flow surrounding the inflow jet. The increase in volume causes a uniform movement of the fluid domain boundary which results in a tangential orientation of the streamlines at the lower ventricle edge. Despite a good qualitative agreement, a quantitative discrepancy of about 10% of the inflow jet itself occurs due to a differing volume flux gradient as plotted in Fig. 7. Figures 9–12 also show 1D velocity profiles for two characteristic positions.

At phase $\varphi_9 = 185^\circ$ the increase in volume drops and the velocity of the intake jet decreases considerably (see Fig. 11), and a thorough mixing in the atrium in form of a vortex in clockwise direction can be seen. As the maximum volume is reached, this clockwise orientation in the atrium initially persists, before the vortex structure collapses because of the decreasing kinetic energy. The ventricle is now in the expulsion phase $\varphi_{14} = 285^\circ$ (Fig. 12).

Hydro-Elastic Quantification

Comparison of the quantitative results in Table 2 show excellent agreement of KaHMo FSI, KaHMo

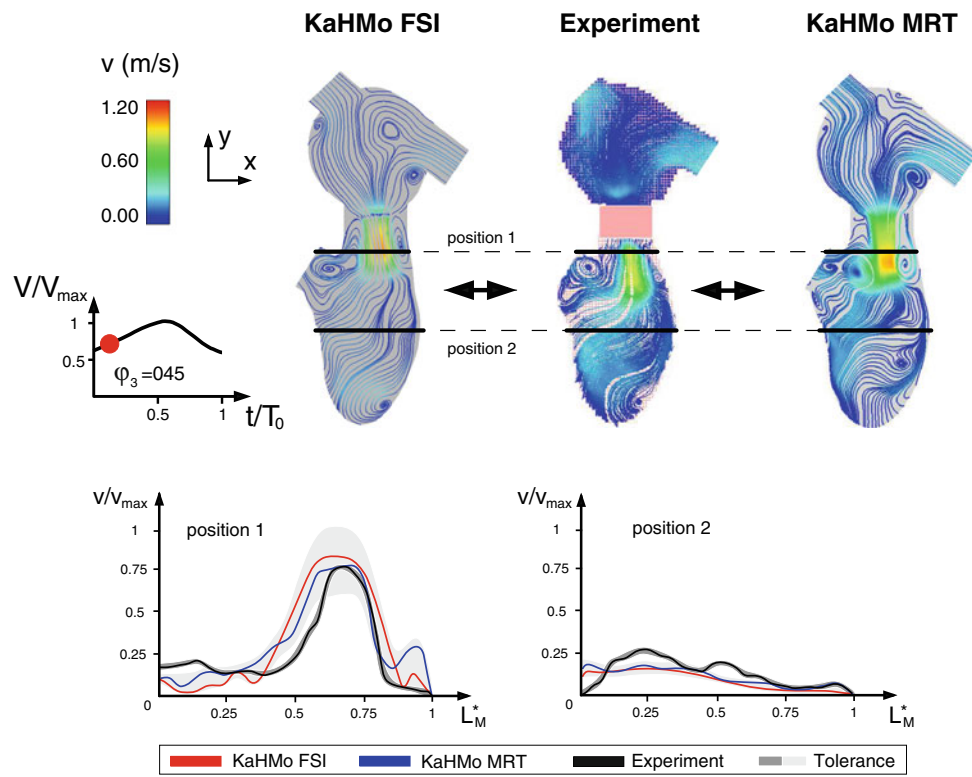


FIGURE 9. Comparison of KaHMo FSI with KaHMo MRT and experimental data in phase $\varphi_3 = 45^\circ$.

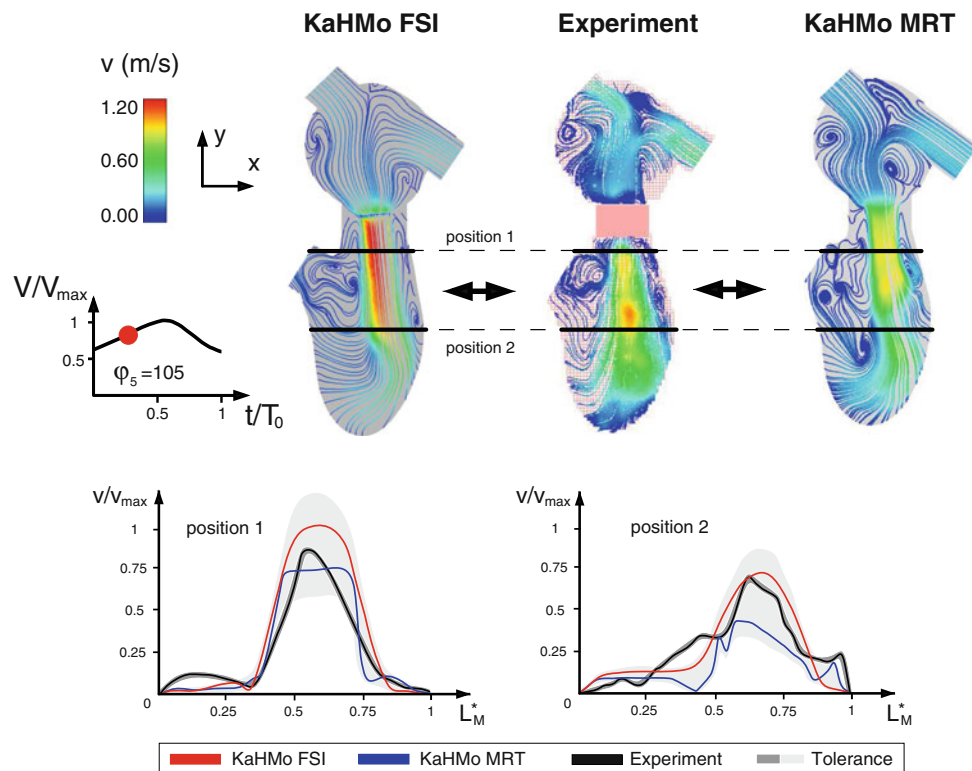


FIGURE 10. Comparison of KaHMo FSI with KaHMo MRT and experimental data in phase $\varphi_5 = 105^\circ$.

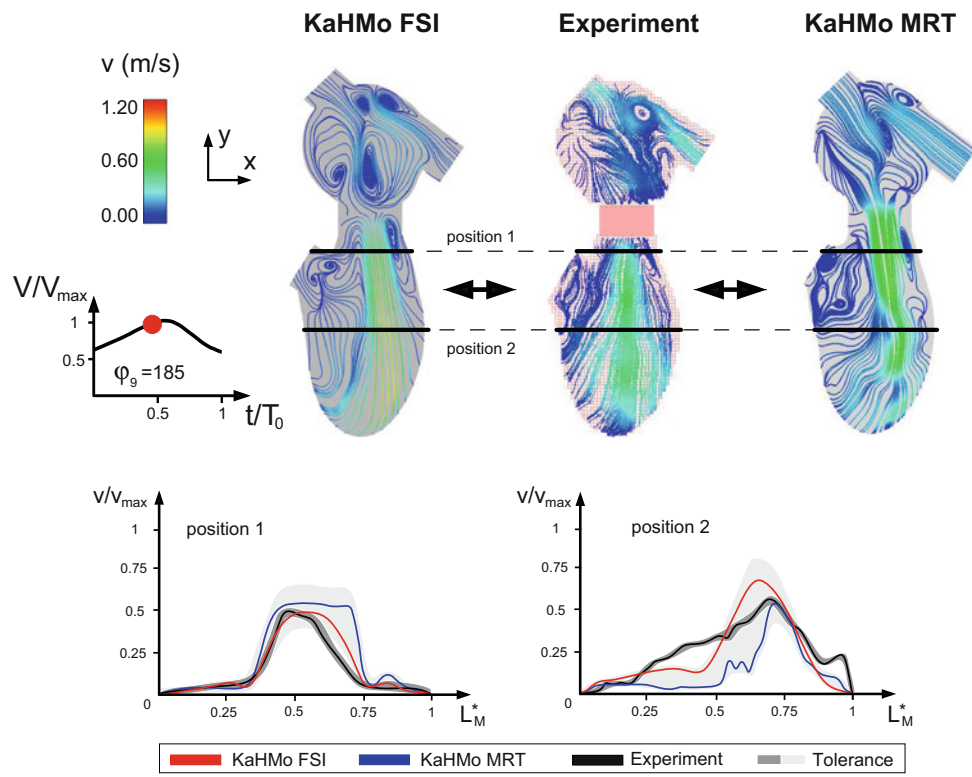


FIGURE 11. Comparison of KaHMo FSI with KaHMo MRT and experimental data in phase $\varphi_9 = 185^\circ$.

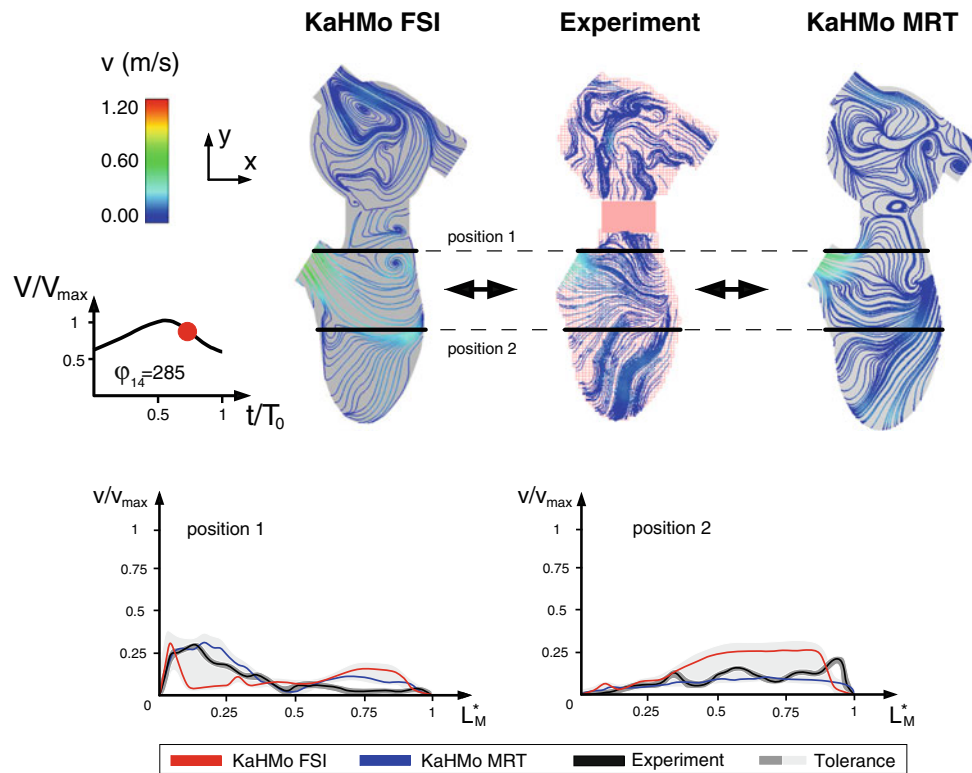


FIGURE 12. Comparison of KaHMo FSI with KaHMo MRT and experimental data in phase $\varphi_{14} = 285^\circ$.

MRT, and experimental findings. Both KaHMo MRT and KaHMo FSI display small deviations in the average speed and the viscosity, which become evident in the characteristic numbers in further analysis. If we take the experimental values as a reference, a deviation of about 5% appears. Using the characteristic fluid mechanical numbers defined in the section “[Evaluation methods](#),” we observe a very good agreement in both Reynolds and Womersley numbers:

Diastole:

$$Re_{FSI}^{dia} = 1427 \leftrightarrow Re_{MRT}^{dia} = 1304 \leftrightarrow Re_{EXP}^{dia} = 1402,$$

$$Wo_{FSI}^{dia} = 17 \leftrightarrow Wo_{MRT}^{dia} = 16 \leftrightarrow Wo_{EXP}^{dia} = 16.$$

Systole:

$$Re_{FSI}^{sys} = 2007 \leftrightarrow Re_{MRT}^{sys} = 1869 \leftrightarrow Re_{EXP}^{sys} = 1947,$$

$$Wo_{FSI}^{sys} = 15 \leftrightarrow Wo_{MRT}^{sys} = 15 \leftrightarrow Wo_{EXP}^{sys} = 15.$$

However, cardiovascular fluid–structure analysis also requires to take characteristic structural properties into account. It should be noted that there is no active contraction included in the structural partition. Consequently, evaluating the diastolic FSI numbers proposed in the section “[Evaluation methods](#),” we obtain the following result

$$\Pi_{FSI}^{E*} = 1 \times 10^0, \quad \Pi_{FSI}^{A*} = 5 \times 10^{-2}, \quad \Pi_{FSI}^{D*} = 7 \times 10^{-4}$$

(scaled (*) with $\Pi_{FSI}^E = 4.14 \times 10^{-2}$).

As far as anatomical heart evaluation is concerned, the passive FSI numbers above correspond to diastolic counterparts observed previously when modeling left ventricular heart models.⁸ Finally, the dimensional cardiac pump work shows very similar characteristics with

$$O_{FSI} = 1.83 \times 10^6 \leftrightarrow O_{MRT} = 1.45 \times 10^6$$

from a fluid mechanics point of view. Table 2 summarizes the most important fluid mechanical input quantities.

DISCUSSION

This study concerns the validation of the FSI heart model KaHMo FSI. A ventricular validation experiment¹⁷ has been reproduced in both fluid and solid mechanical behaviors. Boundary conditions and constitutive behavior have been based on experimental input. The fluid domain deformation is driven by a periodical change of the surrounding pressure, interacting with both structural and fluid-mechanical resistance. Due to the ventricle wall thickness of

approximately 1 mm the choice of a shell-like structural discretization can be justified and has been found adequate given its robustness during the coupled simulation process.

Model Limitations

As far as the comparison of the validation model and real heart function is concerned, we can identify the following limitations. The circulatory system and pump performance of the experimental setup showed a shortcoming in terms of obtaining realistic ejection fraction and Reynolds numbers. This study is therefore restricted to the validation of KaHMo to predict an intra-ventricular flow field rather than representing a physiologically realistic environment. Another consequence of the low ejection fraction is the limitation of the opening of the valves to 73% as shown in Fig. 2. This explains the very good agreement of the intra-ventricular flow fields in Figs. 9–12 as the valves do not extend deeply into the cavity.

As far as the myocardial representation is concerned, the investigation of pressure-driven fluid domain deformation is provided; however, the actual ventricular function is not represented correctly. The experimental cycle starts with an end-systolic configuration widened by a surrounding lower pressure, neglecting contractile input of the atrium. The expulsion phase is represented by the increase in surrounding pressure without internal myocardial contraction. Isochoric phases are restricted to a small pressure change which is also very sensitive in terms of small intra-ventricular pressure variations. The results obtained are sufficient to validate KaHMo FSI’s structural partition.

Pressure–Volume Interaction

Although the structural behavior is represented by a simplified shell-like model, local concave/convex deformation changes observed within the experimental setup are captured nicely by the fluid–solid coupled model. This is confirmed by the good overall agreement of the cavity volume in simulation and measurement plotted over time in Fig. 7. Furthermore, the characteristic end-systolic buckling behavior shown in Fig. 8 is due to fluid inertia and low structural stiffness: In the vicinity of the smallest ventricle volume, a wave-shaped pressure reaction can be seen in Fig. 7. The early filling phase of KaHMo FSI is characterized by a pressure drop, which can be explained by the suction and intake of the fluid. The fluid that is accelerated toward the end of the filling phase causes a pressure increase before the transition to the expulsion phase takes place. The pressure continues to rise,

however, the inner-ventricular fluid needs to be expelled. As soon as the fluid column is set into motion a further pressure drop is observed. The change in volume takes place continuously. Toward the end of the expulsion phase, the pressure load already performs the suction phase. However, the inertia of the out-flowing fluid acts against this change and causes the delayed reaction of the volume change described above. In the intake phase, it is again the fluid inertia that initially acts against an increase in the volume. In order to obtain the resulting change in volume, this inertia must be met by an initial increase in the suction load. This can be neutralized as soon as the incoming fluid has been set into motion. On the other hand the pressure of the coupling model is controlled continuously, but it takes into account the 5% phase shift in specifying the pressure. This explains the small deviation of the change in volume seen in Fig. 8. Overall, an enlarged representation of pV work is predicted by KaHMo FSI.

Flow Field Quality

The comparison of the streamline pattern measured and simulated shows a very good agreement in Figs. 9–12. In the documentation of the experiment, the errors in the PIV data in measurement and evaluation are given as a deviation of about 5%. At the selected flow phases, we observe a very good quantitative agreement between the simulation results and the experimental data. The overall visualization of the flow field helps to understand the complex inner-ventricular flow-pattern from a stand-alone and coupled perspective.

Phase $\varphi_2 = 45$ corresponds to an early stage of the intake process. Both simulation models yield a flow structure that is very similar to the one in the validation experiment. The intake jet is accompanied by a torus-shaped ring vortex. The left part of the vortex is fixed in position by the aortic channel. In addition, there is a good representation of the flow structure in the atrium and apex of the heart. Figure 10 confirms the agreement of the velocity distribution by evaluating the two characteristic 1D profiles. As expected, the maximum velocity occurs just downstream of the inlet diameter. The increase and decrease in the intake velocity during the filling phase can be seen clearly in both sections and also manifests during the expulsion. The uncertainties in the simulation results of KaHMo MRT (blue) and KaHMo FSI (red) of about 20%¹⁷ are due to the tolerance of the CAD geometry as well as the simplified valve models, and give rise to the gray tolerance region.

Figure 10 shows the deep penetration of the intake jet into the ventricle at phase $\varphi_5 = 105^\circ$. There is a very good agreement in the flow pattern in the atrium as well

as in areas surrounding the inflow jet itself. The color coding in Fig. 10 shows that there is a 15% difference of the maximum velocity between KaHMo MRT and KaHMo FSI at this specific point in time. This can be explained as a considerably higher volume flux occurs for $\varphi_5 = 105^\circ$ due to the previous delay and the inflow inertia resistance as we already inferred from Fig. 7.

Although the effects described above can be exhibited in both simulation and experiments, a different flow pattern has been expected. The ring vortex shows a certain movement toward the apex, however, the area toward the left fluid domain boundary appears to be strongly limited. The low ejection fraction does not provide enough momentum to allow the left vortex part to grow, for turning of the ring vortex in the apex of the heart and to dominate the whole cavity, as in the human heart.

Due to the good agreement in volume flux for $\varphi_9 = 185^\circ$ and $\varphi_{14} = 285^\circ$, Figs. 11 and 12 show a flow pattern that is similar for all three streamline visualizations. The velocity profiles show also a good agreement, but there is a slightly higher deviation due to limited accuracy in measurement for small velocities. It should be mentioned that, again, the overall structure is still influenced by the flow pattern discovered in $\varphi_5 = 105^\circ$. A three-dimensional secondary flow arises at the end of the diastole in the mid and lower regions of the ventricle due to the reduced inertia of the fluid. This has an effect on the physiological interpretation of the velocity field as the preferred expulsion region is now in the upper part of the ventricle, whereas the flow through the apex of the ventricle is not optimal.

Quantitative Validation

Characteristic FSI numbers have been evaluated in the section “[Hydro-elastic quantification](#)” to capture the FSI effects quantitatively. First evaluation processes showed the interplay of flow energy, diffusion, and acceleration with structural deformation. One can see that for this validation experiment, characteristic FSI numbers exist for the ventricle filling only as the initial ventricle configuration is represented by the end-systolic shape. Although variations of the simulation need to be performed in order to evaluate and calibrate the numbers proposed, one can already see that the numbers have the same order of magnitude as observed in previous studies.⁸ As expected, physical phenomena can now be described by the dominance of pump energy ($\Pi_{\text{FSI}}^{\text{E}*}$) over acceleration ($\Pi_{\text{FSI}}^{\text{A}*}$), and diffusion ($\Pi_{\text{FSI}}^{\text{D}*}$).

The evaluation of the dimensionless pump work O_{pV} (see Eq. 11) can draw on many years of experience. Figure 13 plots $O_{\text{pV}}^* = O_{\text{pV}}/O_{\text{pV}}^{\text{ref}}$ over ejection

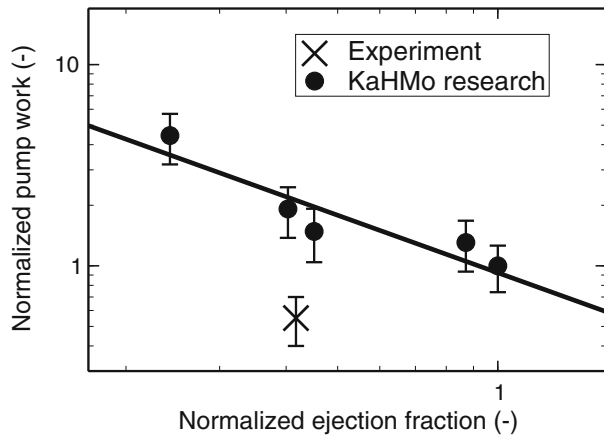


FIGURE 13. Classification of healthy and diseased hearts proposed by Oertel *et al.*¹².

fraction $E^* = E/E^{\text{ref}}$ relative to reference values of a healthy ventricle ($O_{\text{pV}}^{\text{ref}} = 3.4 \times 10^6$, $E^{\text{ref}} = 62\%$). Representative evaluation studies within the KaHMo research series are shown; with logarithmic scales on both axes, a straight line is found, with the linear power law

$$O_{\text{pV}}^* = 1/E^* \quad (15)$$

Healthy hearts are located at the bottom right corner and cardiac dysfunction causes a shift toward the left upper corner (see Oertel *et al.*¹²). After heart attack for instance, the ventricular pumping work decreases but the blood mixing time increases. The dimensionless pumping work assumes larger values than those of a healthy heart. As far as the physiological significance of the validation example is concerned both ejection fraction and pump work need to be taken into account. The former might indicate a representation of an unhealthy object. However, the latter does not correspond to the findings in Fig. 13 as a decrease in ejection fraction must be accompanied by an increase in the dimensionless pump work. In order to represent realistic environment for a ventricular experiment, either the ejection fraction or the pump work must be increased as soon as the limitations discussed above have been overcome.

CONCLUSION AND OUTLOOK

The numerical results of this study have demonstrated that the strength of the KaHMo project lies in the prediction of the inner-ventricular flow field. Although Reynolds number and ejection fraction are not close enough to realistic values, KaHMo FSI was

still able to produce results that are in very good agreement with the ones obtained by both experimental data and KaHMo MRT solutions. In particular, excellent agreement has been obtained in terms of the pressure and volume distribution over time, structural deformation as well as internal flow pattern. Slight discrepancies between KaHMo FSI and KaHMo MRT can be attributed to experimental findings and interpretations. As far as the multi-physics coupling is concerned, we can consider KaHMo FSI in terms of intra-ventricular flow structure and fluid domain deformation.

Future work must aim to locate the validation experiment closer to the connecting evaluation line. The overall agreement of visualized data and quantitative results encourages to further develop the myocardial representation of KaHMo FSI.

It should be noted that the *in vivo* evaluation of computational models—especially cardiovascular blood flow—is still a challenge. Due to the lack of patient-specific information, current validation procedures need to focus on experimental studies as presented within this study. However, with the continuous progress in medical imaging techniques, KaHMo research will soon be able to undertake more physiologically significant evaluation based on myocardial muscle models. MRI phase mapping procedures for both tissue⁵ and blood flow¹¹ provide a comprehensive quantitative analysis of myocardial velocities with high temporal and spatial resolution. Diffusion tensor MRI techniques²¹ will provide important input in terms of myocardial fiber orientation. This will help us to further evaluate existing FSI models and to apply KaHMo FSI to clinically relevant problems to improve the understanding of cardiac disease and its treatment. An exact understanding of regional myocardial performance and blood flow interaction is an essential prerequisite for the diagnosis of heart disease. The ultimate goal of the KaHMo research effort is to provide patient-specific analysis rather than feasibility study results.

ACKNOWLEDGMENTS

The authors express their sincere gratitude to all contributors to the KaHMo project during recent years. Especially to Dr.-Ing. Kathrin Spiegel for providing simulation reference data as well as Professor Dr.-Ing. habil. Dieter Liepsch (University of Applied Science, Munich) for providing experimental input for both KaHMo MRT and KaHMo FSI. Part of this study was supported by the Deutsche Forschungsgesellschaft (DFG-Project OE 86/24-1).

REFERENCES

- ¹Baccani, B., F. Domenichini, and G. Pedrizzetti. Model and influence of mitral valve opening during the left ventricular filling. *J. Biomech.* 36:335–361, 2003.
- ²Cheng, Y., H. Oertel, and T. Schenkel. Fluid-structure coupled 3D CFD simulation of the left ventricular flow during filling phase. *Ann. Biomed. Eng.* 33(5):567–576, 2005.
- ³Janoske, U., G. Silber, R. Kröger, M. Stanull, G. Benderoth, T. Schmitz-Rixen, T. J. Vogel, and R. Moosdorf. *Fluid-structure interaction in abdominal aortic aneurysms.* 7th MpCCI User Conference, 2006.
- ⁴Jones, T. N., and D. N. Netaxas. Patient-specific analysis of left ventricular blood flow. *Comput. Sci.* 1496:154–166, 1998.
- ⁵Jung, B. A., B. W. Kreher, M. Markl, and J. Hennig. Visualization of tissue velocity data from cardiac wall motion measurements with myocardial fibre tracking: principles and implications for cardiac fiber structure. *Eur. J. Cardiothor. Surg.* 29(1):158–164, 2006.
- ⁶Kilner, P.J., G.-Z. Yang, A. J. Wilkes, R. H. Mohiaddin, D. N. Firmin, and M. H. Yacoub. Asymmetric redirection of flow through the heart. *Nature* 404:759–761, 2000.
- ⁷Krittian, S. Modellierung der kardialen Strömungs-Struktur-Wechselwirkung. Dissertation, Institute for Fluid Mechanics, University of Karlsruhe (TH), Germany, 2009.
- ⁸Krittian, S., U. Janoske, H. Oertel, and T. Böhlke. Partitioned fluid solid coupling for cardiovascular blood flow: left-ventricular fluid mechanics. *Ann. Biomed. Eng.* doi: [10.1007/s10439-009-9895-7](https://doi.org/10.1007/s10439-009-9895-7). ISSN:0090-6964 (Print) 1573-9686 (Online), 2010.
- ⁹Liepsch, D., G. Thurston, and M. Lee. Studies of fluids simulating blood-like rheological properties and applications in models of arterial branches. *Biorheology* 28(1–2): 39–52, 1991.
- ¹⁰Long, Q., R. Merrifield, G.-Z. Yang, X. Y. Xu, P. J. Kilner, and D. N. Firmin. The influence of inflow boundary conditions on intra left ventricle flow predictions. *J. Biomech. Eng.* 125:922–927, 2003.
- ¹¹Michael, M., A. Harloff, T. A. Bley, M. Zaitsev, B. Jung, E. Weigang, M. Langer, J. Hennig, and A. Frydrychowicz. Time-resolved 3D MR velocity mapping at 3T: Improved navigator-gated assessment of vascular anatomy and blood flow. *J. Magn. Reson. Imag.* 25(4):824–831, 2007.
- ¹²Oertel, H., S. Krittian, and K. Spiegel. Modeling the Human Cardiac Fluid Mechanics, 3rd ed. Karlsruhe University Press, 2009.
- ¹³Pedrizzetti, G., and F. Domenichini. Nature optimizes the swirling flow in the human left ventricle. *Phys. Rev. Lett.* 95(10):108101, 2005.
- ¹⁴Penrose, J. M. T., and C. J. Staples. Implicit fluid-structure coupling for simulation of cardiovascular problems. *Int. J. Numer. Methods Fluids* 40:467–478, 2002.
- ¹⁵Saber, N. R., N. B. Wood, A. D. Gosman, R. D. Merrifield, G. Z. Yang, C. L. Charrier, P. D. Gatehouse, and D. N. Firmin. Progress towards patient-specific computational flow modelling of the left heart via combination of magnetic resonance imaging with computational fluid dynamics. *Ann. Biomed. Eng.* 31(1):42–52, 2003.
- ¹⁶Schenkel, T., M. Malve, M. Reik, M. Markl, B. Jung, and H. Oertel. MRI based CFD analysis of flow in a human left ventricle. Methodology and application to a healthy heart. *Ann. Biomed. Eng.* 37(3):503–515, 2009.
- ¹⁷Spiegel, K. Strömungsmechanischer Beitrag zur Planung von Herzoperationen. Ph.D. thesis, Institute for Fluid Mechanics, University of Karlsruhe (TH), 2009.
- ¹⁸Spiegel, K., T. Schmid, T. Schenkel, and H. Oertel. Validierung des Karlsruher Herzmodells (DFG-Projekt OE 86/24-1). Technical report; Institute for Fluid Mechanics, University of Karlsruhe (TH), 2008.
- ¹⁹Walker, P. G., G. B. Cranney, R. Y. Grimes, J. Delatore, J. Rectenwald, G. M. Pohost, and A. P. Yoganathan. Three-dimensional reconstruction of the flow in a human left heart by using magnetic resonance phase velocity encoding. *Ann. Biomed. Eng.* 24(1):139–147, 1996.
- ²⁰Watanabe, H., S. Sugiura, H. Kafuku, and T. Hisada. Multiphysics simulation of left ventricular filling dynamics using fluid-structure interaction finite element method. *Biophys. J.* 87:2074–2085, 2004.
- ²¹Zhukov, L., and A. H. Barr. Heart-muscle fiber reconstruction from diffusion tensor MRI. *IEEE Visual.* 597–602, 2003.
- ²²<http://www.simulia.com>.
- ²³<http://www.fluent.com>.
- ²⁴<http://www.mpcci.de>.